GEOPHYSICS, VOL. 86, NO. 3 (MAY-JUNE 2021); P. R277–R292, 18 FIGS., 1 TABLE.
10.1190/GEO2020-0286.1

High-frequency localized elastic full-waveform inversion for time-lapse seismic surveys

Shihao Yuan[1], Nobuaki Fuji[2], and Satish C. Singh[2]

ABSTRACT

Seismic full-waveform inversion (FWI) is a powerful method used to estimate the elastic properties of the subsurface. To mitigate the nonlinearity and cycle-skipping problems, in a hierarchical manner, one first inverts the low-frequency content to determine long- and medium-wavelength structures and then increases the frequency content to obtain detailed information. However, the inversion of higher frequencies can be computationally very expensive, especially when the target of interest, such as oil/gas reservoirs and axial melt lens, is at a great depth, far away from source and receiver arrays. To address this problem, we have developed a localized FWI algorithm in which iterative modeling is performed locally, allowing us to extend inversions for higher frequencies with little computation effort. Our method is particularly useful for time-lapse seismic, where the changes in elastic parameters are local due to fluid extraction and injection in the subsurface. In our method, the sources and receivers are extrapolated to a region close to the target area, allowing forward modeling and inversion to be performed locally after low-frequency full-model inversion for the background model, which by nature only represents long- to medium-wavelength features. Numerical tests show that the inversion of low-frequency data for the overburden is sufficient to provide an accurate high-frequency estimation of elastic parameters of the target region.

INTRODUCTION

In some geophysical applications, such as reservoir monitoring, it is indispensable to obtain the temporal changes of the subsurface for optimization of borehole placement, maximization of hydrocarbon recovery, and its associated cost reduction (Snieder et al., 2007; Jack, 2017). To detect these temporal changes, we need to repeatedly conduct seismic surveys. This technique is generally referred to as time lapse or 4D seismic. During the past decades, 4D seismic surveys have evolved from a field experiment to a practical reservoir monitoring tool that can add significant value to oil and gas production (Lumley, 2004; Landrø, 2006). With the increasing hydrocarbon consumption and the depletion of many old fields, enhanced oil/gas recovery techniques such as 4D seismic have become more beneficial, especially in areas where the cost and risks of drilling are very high. Additional oil/gas detected with 4D seismic is relatively cheap to produce due to the existing platform.

The 4D seismic poses challenges for acquisition and data processing. To acquire the time-lapse seismic response that is purely caused by subsurface changes, such as fluid movement/replacement or pore pressure changes, we are supposed to conduct highly repeatable seismic surveys (Eriksrud, 2014). Early 4D seismic studies mainly focus on a limited portion of the whole seismic wavefields to estimate subsurface changes, such as time shift and amplitude variation versus offset (Landrø and Stammeijer, 2004). Although these techniques benefit from their fast and robust algorithm, they are mostly restricted to simple models (e.g., a two-layer model with an overburden and a reservoir) with ray-based forward modeling, which is hardly valid in complex geologic structures. Improved acquisition technologies (with acceptable repeatability and sensitivity) are offering a new opportunity to develop full-waveform-based methods for 4D seismic. Full-waveform inversion (FWI) has been gradually and successfully integrated into 4D seismic analysis

Manuscript received by the Editor 2 May 2020; revised manuscript received 4 December 2020; published ahead of production 19 January 2021; published online 18 March 2021.
[1]Ludwig-Maximilians-Universität München, Department of Earth and Environment Sciences, Munich, 80333, Germany and Université de Paris, Institut de physique du globe de Paris, CNRS, Paris F-75005, France. E-mail: syuan@geophysik.uni-muenchen.de (corresponding author).
[2]Université de Paris, Institut de physique du globe de Paris, CNRS, Paris F-75005, France. E-mail: nobuaki@ipgp.fr; singh@ipgp.fr.
© 2021 Society of Exploration Geophysicists. All rights reserved.

Downloaded from http://pubs.geoscienceworld.org/geophysics/article-pdf/doi/10.1190/geo2020-0286.1/5256644/geo-2020-0286.1.pdf
by CNRS INSU user

(Zheng et al., 2011; Queißer and Singh, 2013; Raknes and Arntsen, 2015; Hicks et al., 2016; Yang et al., 2016).

Since the pioneering work of Lailly (1983) and Tarantola (1984), FWI has proven its strength in providing high-resolution quantitative images of subsurface structures (Pratt, 1999; Shipp and Singh, 2002; Virieux and Operto, 2009). FWI retrieves the estimated earth models recursively by seeking to match synthetic waveforms to observed waveforms. However, it is well known that elastic waveform inversion is computationally demanding. The cost of solving the elastic wave equation depends on the size of the discrete models using any numerical method. For practical-scale problems, the discretized models often consist of billions of grid points in space and thousands of steps in time. Although the increasing availability of high-performance computers allows us to perform 3D elastic waveform inversion in real cases (Hicks et al., 2016; Hoeber et al., 2017; Marjanović et al., 2018), it is still challenging in 4D seismic for repeated experiments. Meanwhile, the total number of spatial and temporal grid points will approximately scale to the fourth power of the frequency for the inversion. Therefore, the computational cost in terms of computing time and memory will grow sharply if we pursue a high-frequency waveform inversion, which necessitates increasingly denser spatial and temporal grids to avoid numerical dispersion and stability problems.

For 4D seismic studies, our area of interest is likely to be restricted to the reservoir and its immediate surroundings, which are generally much smaller than the full background medium. Localized waveform inversion only within the domain of interest will thus be useful to mitigate the computational cost encountered with 4D seismic. Reservoir monitoring is normally implemented in the process of production after the exploration stage whereby the baseline model is supposed to be known. The acquired baseline model (e.g., through baseline waveform inversion) enables wavefield simulations solely inside the target region. Recent research on localized waveform inversion reveals that such a strategy has the potential to be applied to practical 4D elastic waveform inversion with significantly reduced computational cost compared to conventional full-model waveform inversion (Haffinger et al., 2013; Borisov et al., 2015; Malcolm and Willemsen, 2016; Masson and Romanowicz, 2017; Willemsen and Malcolm, 2017; Yuan et al., 2017a, 2017b).

Hybrid solvers have been proposed to improve the efficiency of wavefield simulations (Capdeville et al., 2003). Monteiller et al. (2012, 2015) combine the direct solution method for teleseismic waves outside the target area with a more accurate 3D spectral element solver within the area of interest. Willemsen and Malcolm (2017) introduce a local elastic solver that is accurate for recovering reservoir properties while using an acoustic solver to propagate the wavefield to the subdomain. Haffinger et al. (2013) propose to perform localized inversion after source- and receiver-side wavefield extrapolation. This approach poses a requirement on spatial samplings of sources and receivers to avoid aliasing problems. Moreover, a proper time window has to be set up to exclude the spurious events caused by wavefield extrapolation. Borisov et al. (2015) first introduce the wavefield injection method to localized inversion problems and achieve a promising efficiency, but they assume that the data are directly recorded in the subsurface above the target depth. Yuan et al. (2017a) present a methodology to perform waveform inversion through combining source-side wavefield injection and receiver-side extrapolation methods. Malcolm and Willemsen (2016) develop a frequency-domain localized inversion technique that is based on the exact boundary condition (van Manen et al., 2007; Broggini et al., 2017). This technique is theoretically more accurate than the wavefield injection method, but it is computationally more demanding (Masson and Romanowicz, 2017). Because the exact boundary condition requires computation and storage of the Green's functions of all possible pairs of boundary points (van Manen et al., 2007), the extension of the methodology to higher dimensions (two or three dimensions) in elastic media will require a much larger number of Green's functions, which will eventually require additional efficient algorithms to tackle this problem. Furthermore, it is still not thoroughly studied how the errors in baseline models affect localized simulations using the exact boundary condition. To our knowledge, most of the existing works on localized waveform inversions are based on acoustic assumptions and/or 2D examples, which are important but limited by the approximations used.

Considering the above aspects, we use the wavefield injection method as the localized numerical solver in this study. We estimate the accuracy and efficiency of the proposed localized elastic waveform inversion using more realistic 2D and 3D synthetic examples. We apply the scale separation concept (Claerbout, 1985; Jannane et al., 1989) and show the effectiveness and accuracy of a hierarchical elastic localized waveform inversion strategy that starts with a low-frequency and long-offset (<10 Hz) baseline elastic waveform inversion to recover the background model, followed by a high-frequency (up to 40 Hz) localized elastic waveform inversion that seeks to quantitatively invert small-scale perturbations. In baseline waveform inversions, using low-frequency data helps to reduce the computational cost due to relatively sparse grid spacing and long-offset data ensure the sensitivity to the long- and medium-wavelength structures. The repeated high-frequency localized waveform inversion will further reduce computational costs because the modeling is restricted to a smaller region.

The paper is organized as follows. In the "Methodology" section, we review the theoretical basis of localized FWI. We then examine the proposed workflows through 2D and 3D synthetic experiments using various models. Finally, we discuss challenges that may arise in real experiments and perspectives of imaging remote target regions for exploration and global tomographic problems.

METHODOLOGY

Although the localized inversion scheme has been introduced in Yuan et al. (2017a), here we regroup the wavefield injection and extrapolation methods with a consistent notation so that the assumptions made for source- and receiver-sides are clear. We first review the time-lapse elastic waveform inversion in the time domain with a double-difference misfit function. The key element of the localized inversion is the forward simulation using the wavefield injection method, which requires a local expression for the physical sources and receivers. Therefore, we recall the reciprocity-based representation theorem and the associated boundary integral in the application to time-lapse wavefield simulation and extrapolation for completeness.

Forward modeling

We begin with the equation of motion for a given model in the time domain to simplify the following discussion:

$$\rho^0(\mathbf{x},t)\ddot{u}_i^0(\mathbf{x},t) - [(C_{ijkl}^0(\mathbf{x},t)u_{k,l}^0(\mathbf{x},t)]_{,j} = f_i(t), \quad (1)$$

Downloaded from http://pubs.geoscienceworld.org/geophysics/article-pdf/doi/10.1190/geo2020-0286.1/5256644/geo-2020-0286.1.pdf
by CNRS INSU user

where ρ is the density, u_i is the ith component of displacement, C_{ijkl} are the elastic tensor components, and f_i is the ith component of the external body force. The subscript i denotes the spatial partial derivative with respect to the ith direction, and the double dots over the variables denote the second-order partial derivative with respect to time. The superscript 0 represents wavefields for the baseline models. The subscripts represent indices of components in Cartesian coordinates, and Einstein's convention is valid only for the subscripts. We use a time-domain finite-difference staggered-grid scheme (Virieux, 1986), fourth-order in space and second-order in time $\mathcal{O}(dx^4, dt^2)$ (Graves, 1996; Borisov and Singh, 2015). In the $\mathcal{O}(dx^4, dt^2)$ finite-difference scheme, one requires a minimum of five grid points per shortest wavelength for accurate modeling (Levander, 1988):

$$f_{\max} < \frac{V_{\min}}{5\Delta x}, \tag{2}$$

where $f_{\max}$ denotes the maximum frequency to be modeled and $V_{\min}$ is the minimum velocity of the model. Meanwhile, the stability condition is satisfied when

$$\Delta t \le \frac{6\Delta x}{7\sqrt{3}V_{\max}}, \tag{3}$$

where $V_{\max}$ denotes the maximum compressional wave (P-wave) velocity (Yao and Margrave, 2000). The computational cost of forward modeling is directly related to the total number of grid points in the discrete model. To compute wavefields at higher frequencies (greater than 40 Hz) while avoiding numerical dispersion and stability problems, we are supposed to use finer grids that might be computationally prohibitive in practical-scale problems. Unsplit convolutional perfectly matched layers are used to decrease our modeling area in localized waveform inversion and absorb undesirable reflections from the reduced model boundaries (Komatitsch and Martin, 2007).

Inverse problem

The localized time-lapse waveform inversion allows us to naturally apply a double-difference strategy (Waldhauser and Ellsworth, 2000; Zheng et al., 2011; Asnaashari et al., 2015; Yang et al., 2015). Let the synthetic data $\mathbf{u}^0 = \mathbf{u}(\mathbf{m}^0)$ calculated for a baseline model $\mathbf{m}^0$ and $\mathbf{u}^0 + \mathbf{u}^1 = \mathbf{u}(\mathbf{m}^0 + \mathbf{m}^1)$ for a time-lapse model to be inverted $(\mathbf{m}^0 + \mathbf{m}^1)$. We seek the model perturbation $\mathbf{m}^1$ by comparing the baseline observed data $\mathbf{d}^0$ and the monitor observed data $(\mathbf{d}^0 + \mathbf{d}^1)$. We undertake the classic least-squares objective function J to iteratively minimize the difference between modeled $\mathbf{u}^1$ and observed differential wavefield $\mathbf{d}^1$ to obtain $\mathbf{m}^1$:

$$J(\mathbf{m}^1) = \frac{1}{2}(\mathbf{u}^1 - \mathbf{d}^1)^t(\mathbf{u}^1 - \mathbf{d}^1), \tag{4}$$

where the superscript t denotes the transpose of matrices and vectors. Note that the data vectors are gathered for all of the physical and/or virtual sources and receivers, including all of the body-wave phases. We apply the conjugate gradient method to update the model using the following expression:

$$\mathbf{m}_p^1 = \mathbf{m}_{p-1}^1 - \alpha_p \mathbf{g}_p^c(\mathbf{m}_p^1) \quad \text{for } p \ge 1, \tag{5}$$

where α denotes the model-updating step length and p is the number of iterations. The conjugate-gradient direction $\mathbf{g}^c$ is obtained from the current and previous gradient of the objective function as follows (Polak, 1971):

$$\begin{aligned} \mathbf{g}_p^c &= \mathbf{g}_p && \text{for } p = 1, \\ \mathbf{g}_p^c &= \mathbf{g}_p + \frac{\mathbf{g}_p^T(\mathbf{g}_p - \mathbf{g}_{p-1})}{\mathbf{g}_p^T\mathbf{g}_p}\mathbf{g}_{p-1} && \text{for } p > 1. \end{aligned} \tag{6}$$

The step length α is defined as (Pica et al., 1990)

$$\begin{aligned} \alpha_p &= \epsilon \frac{[\mathbf{u}_p^{(1,\epsilon)} - \mathbf{u}_p^1]^t[\mathbf{u}_p^1 - \mathbf{d}^1]}{[\mathbf{u}_p^{(1,\epsilon)} - \mathbf{u}_p^1]^t[\mathbf{u}_p^{(1,\epsilon)} - \mathbf{u}_p^1]} \\ &= \epsilon \frac{[\mathbf{u}(\mathbf{m}^0 + \mathbf{m}_p^1 + \epsilon\mathbf{g}_p) - \mathbf{u}(\mathbf{m}^0 + \mathbf{m}_p^1)]^t[\mathbf{u}(\mathbf{m}^0 + \mathbf{m}_p^1) - \mathbf{u}^0 - \mathbf{d}^1]}{[\mathbf{u}(\mathbf{m}^0 + \mathbf{m}_p^1 + \epsilon\mathbf{g}_p) - \mathbf{u}(\mathbf{m}^0 + \mathbf{m}_p^1)]^t[\mathbf{u}(\mathbf{m}^0 + \mathbf{m}_p^1 + \epsilon\mathbf{g}_p) - \mathbf{u}(\mathbf{m}^0 + \mathbf{m}_p^1)]}, \end{aligned} \tag{7}$$

where $\mathbf{u}_p^{(1,\epsilon)}$ is the synthetic time-lapse data difference generated for a slightly perturbed model along the gradient direction at current iteration $(\mathbf{m}^0 + \mathbf{m}_p^1 + \epsilon\mathbf{g}_p)$ with ϵ as the scaling factor. The calculation of equation 7 of the step length requires one extra forward modeling for $\mathbf{u}_p^{(1,\epsilon)}$ at each iteration. The choice of ϵ is generally to make the maximum P-wave velocity perturbation <1.0%. The gradient vectors in equations 5 and 6 are evaluated based on the adjoint-state method (Geller and Hara, 1993; Liu and Tromp, 2006; Plessix, 2006), leading to

$$\mathbf{g}_p = \nabla_{\mathbf{m}_p} J_p = \sum_{\mathbf{r}_R, \mathbf{r}_S} \mathbf{g}_p(\mathbf{r}_R, \mathbf{r}_S). \tag{8}$$

The gradient term $\mathbf{g}_p(\mathbf{r}_R, \mathbf{r}_S)$, contributed from each source $\mathbf{r}_S$ and receiver $\mathbf{r}_R$ pair, can be obtained as

$$\begin{aligned} \mathbf{g}_p(\mathbf{r}_R, \mathbf{r}_S)\delta\mathbf{m} = &\int_{-\infty}^{\infty} d\tau \int_V dV \delta\rho \dot{\mathbf{u}}(\tau; \mathbf{r}_S) \cdot \dot{\boldsymbol{\eta}}(T - \tau; \mathbf{r}_R) \\ &+ \int_{-\infty}^{\infty} d\tau \int_V dV \nabla\mathbf{u}(\tau; \mathbf{r}_S) : \delta\mathbf{C} : \nabla\boldsymbol{\eta}(T - \tau; \mathbf{r}_R), \end{aligned} \tag{9}$$

where T denotes the interval of the recorded time series, V denotes the volume of the whole medium, $\delta\rho$ and $\delta\mathbf{C}$ denote a unit perturbation, and the symbol : denotes the double scalar product, that is, $(\mathbf{C} : \nabla\boldsymbol{\eta})_{ij} = C_{ijkl}\partial_k\eta_l$. We omit spatial dependencies for the sake of readability. The adjoint wavefield $\boldsymbol{\eta}$ from $\mathbf{r}_R$ with a time-reversed source-time function $(\mathbf{u}^1 - \mathbf{d}^1)$ can be derived from

$$\begin{aligned} &\rho\ddot{\boldsymbol{\eta}} - \nabla \cdot (\mathbf{C} : \nabla\boldsymbol{\eta}) \\ &\quad = \sum_{\mathbf{r}_R} \delta(\mathbf{x} - \mathbf{r}_R)[\mathbf{u}^1(\mathbf{m}, \mathbf{r}_R, T - \tau) - \mathbf{d}^1(\mathbf{r}_R, T - \tau)]. \end{aligned} \tag{10}$$

In an elastic isotropic medium, the gradients of the objective function with respect to the Lamé parameters λ and μ can be written as, respectively,

Downloaded from http://pubs.geoscienceworld.org/geophysics/article-pdf/doi/10.1190/geo2020-0286.1/5256644/geo-2020-0286.1.pdf
by CNRS INSU user

$$\mathbf{g}(\lambda) = \sum_{\mathbf{r}_R, \mathbf{r}_S} \int_{-\infty}^{\infty} d\tau \int_V dV[(\nabla \cdot \mathbf{u})(\nabla \cdot \boldsymbol{\eta})],$$
$$\mathbf{g}(\mu) = \sum_{\mathbf{r}_R, \mathbf{r}_S} \int_{-\infty}^{\infty} d\tau \int_V dV[(\nabla \boldsymbol{\eta}) : (\nabla \mathbf{u}) + (\nabla \boldsymbol{\eta}) : (\nabla \mathbf{u})^t]. \tag{11}$$

Because Lamé parameters are hardly resolved (Tarantola, 1986), the gradient expression in equation 11 is normally converted to the P-wave and shear wave (S-wave) velocity gradients (Mora, 1987), written as, respectively,

$$\mathbf{g}(V_P) = 2\rho V_P \mathbf{g}(\lambda), \quad \mathbf{g}(V_S) = -4\rho V_S \mathbf{g}(\lambda) + 2\rho V_S \mathbf{g}(\mu). \tag{12}$$

The update of density parameters is linearly linked to the V_P model at the current iteration through Gardner's relationship (Gardner et al., 1974). Using the gradient and step-length expressions given in equations 7–12, the P- and S-wave velocities can be updated simultaneously and independently at each iteration.

Representation theorem for time-lapse wavefield simulation and extrapolation

Here, we briefly review the representation theorem for a perturbed wavefield due to a local perturbation occurring only inside a small region V^+ (Figure 1). We are especially interested in finding an efficient and accurate expression for the modeled $\mathbf{u}^1$ and observed $\mathbf{d}^1$ scattered wavefield, which are recorded at subsurface virtual receivers due to model alterations in a target area. Based on the representation theorem (Knopoff and Gangi, 1959; Wapenaar and Fokkema, 2006), in the case of unperturbed models (Figure 1a), we can express the wavefield inside the volume of interest V^+ as

$$u_n^0(\mathbf{x}_B, t; \mathbf{x}_A) = \int_{-\infty}^{\infty} d\tau \oint_{\partial V^+} dS[G_{in}^0(\mathbf{x}, \tau; \mathbf{x}_B)(C_{ijkl}^0 u_{k,l}^0(\mathbf{x}, t - \tau; \mathbf{x}_A))_{,j} - u_i^0(\mathbf{x}, t - \tau; \mathbf{x}_A)(C_{ijkl}^0 G_{kn,l}^0(\mathbf{x}, \tau; \mathbf{x}_B))_{,j}]s_j, \quad (\mathbf{x}_B \in V^+), \tag{13}$$

and the outside wavefield in the area of V^- as

$$u_n^0(\mathbf{x}_B, t; \mathbf{x}_A) = \int_{V^-} dV f_i G_{in}^0(\mathbf{x}_B, t; \mathbf{x}) + \int_{-\infty}^{\infty} d\tau \oint_{\partial V^+} dS[G_{in}^0(\mathbf{x}, \tau; \mathbf{x}_B)(C_{ijkl}^0 u_{k,l}^0(\mathbf{x}, t - \tau; \mathbf{x}_A))_{,j} - u_i^0(\mathbf{x}, t - \tau; \mathbf{x}_A)(C_{ijkl}^0 G_{kn,l}^0(\mathbf{x}, \tau; \mathbf{x}_B))_{,j}]s_j, \quad (\mathbf{x}_B \in V^-), \tag{14}$$

with the Green's functions satisfying

$$\rho(\mathbf{x}, t)\ddot{G}_{in}(\mathbf{x}, t; \mathbf{x}_A) - [(C_{ijkl}(\mathbf{x}, t)G_{kn,l}(\mathbf{x}, t; \mathbf{x}_A)]_{,j} = \delta_{in}\delta(t)\delta(\mathbf{x} - \mathbf{x}_A), \tag{15}$$

where V^+ denotes the target area, $\partial V^{-/+}$ denotes the surrounding surface of the target area, and s_j is the outward pointing normal vector of the corresponding integral boundary. In our numerical scheme, we store beforehand the particle velocity and traction wavefield field along the surface $\partial V^{+/-}$ that encloses the target area within the baseline model $\mathbf{m}^0$. This requires that we perform a series of forward modeling steps in the full baseline model, where the number of simulations equals the number of physical shots.

The stored boundary wavefield will be treated as the body-force equivalence (boundary conditions) used for driving the localized wavefield reconstructions. This equivalence forms the theoretical basis of the wavefield injection method (Robertsson and Chapman, 2000; Masson et al., 2013) used in this study. In the case of perturbed models (Figure 1b), the modeled wavefield inside the volume V^- can be expressed as

$$\begin{aligned}(u_n^0 + u_n^1)(\mathbf{x}_B, t; \mathbf{x}_A) &= \int_{V^-} dV G_{in}^0(\mathbf{x}, t; \mathbf{x}_B) f_i \\ &+ \int_{-\infty}^{\infty} d\tau \oint_{\partial V^-} dS[G_{in}^0(\mathbf{x}, \tau; \mathbf{x}_B)((C_{ijkl}^0 + C_{ijkl}^1)(u_{kn,l}^0 + u_{kn,l}^1))_{,j} \quad (\mathbf{x}, t - \tau; \mathbf{x}_A) \\ &- (u_n^0 + u_n^1)(\mathbf{x}, t - \tau; \mathbf{x}_A)(C_{ijkl}^0 G_{kn,l}^0(\mathbf{x}, \tau; \mathbf{x}_B))_{,j}]s_j, \quad (\mathbf{x}_B \in V^-).\end{aligned} \tag{16}$$

Subtracting equation 14 from equation 16 for each side, and using the fact that $C_{ijkl}^1 = 0$ everywhere inside V^-, we obtain

$$u_n^1(\mathbf{x}_B, t; \mathbf{x}_A) = \int_{-\infty}^{\infty} d\tau \oint_{\partial V^-} dS[G_{in}^0(\mathbf{x}, \tau; \mathbf{x}_B) C_{ijkl}^0 u_{k,l}^1(\mathbf{x}, t - \tau; \mathbf{x}_A) - u_n^1(\mathbf{x}, t - \tau; \mathbf{x}_A) C_{ijkl}^0 G_{kn,l}^0(\mathbf{x}, \tau; \mathbf{x}_B)]s_j. \tag{17}$$

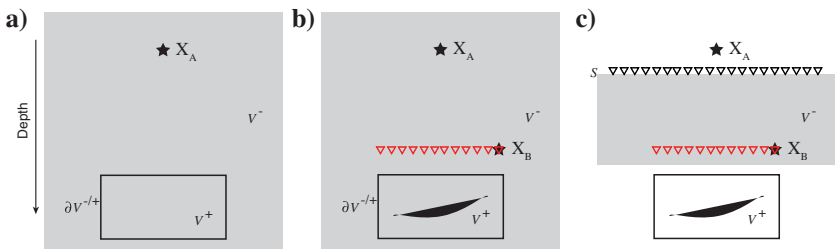


Figure 1. A schematic illustration of the representation theorem. The star X_A denotes the physical source position. The black and red triangles denote the physical and virtual receiver positions, respectively. The term V^+ inside the solid square is the target area, and V^- is the outside area. (a) Modeling wavefield within V^+ (equation 13) or V^- (equation 14) in the case of an unperturbed model. (b) Modeling scattered wavefield recorded at virtual receivers caused by local perturbations within V^+ using equation 17. (c) Extrapolating wavefield from physical receivers (recorded at the earth surface or ocean bottom S) to virtual receivers using equation 18.

Downloaded from http://pubs.geoscienceworld.org/geophysics/article-pdf/doi/10.1190/geo2020-0286.1/5256644/geo-2020-0286.1.pdf
by CNRS INSU user

The derived $\mathbf{u}^1(\mathbf{x}_B, \mathbf{x}_A)$ will serve as the modeled scattered wavefield at the virtual receivers (for more details on the wavefield injection method, see Robertsson and Chapman, 2000; Opršal et al., 2009). For the receiver side, to extrapolate time-lapse data differences from physical to virtual receivers (Figure 1c), we only need to apply the time reversal invariance principle (Bojarski, 1983; Fink et al., 2000). Applying a time reversal to the source $\mathbf{x}_B$ at subsurface virtual receivers, that is, changing the convolution operators to crosscorrelation operators and replacing $\mathbf{u}^1$ with $\mathbf{d}^1$, we obtain

$$d_n^1(\mathbf{x}_B, t; \mathbf{x}_A) \approx \int_{-\infty}^{\infty} d\tau \int_S dS[-G_{in}^0(\mathbf{x}, \tau; \mathbf{x}_B) C_{ijkl}^0 d_{k,l}^1(\mathbf{x}, t+\tau; \mathbf{x}_A) - d_n^1(\mathbf{x}, t+\tau; \mathbf{x}_A) C_{ijkl}^0 G_{kn,l}^0(\mathbf{x}, \tau; \mathbf{x}_B)] s_j, \quad (18)$$

where S denotes the physical receiver plane on the earth surface or ocean bottom (truncated ∂V^-) and $\mathbf{d}_n^1(\mathbf{x}_B, \mathbf{x}_A)$ denotes the extrapolated time-lapse data differences at virtual receivers, serving as the observed wavefield in the proposed localized FWI scheme. The use of the approximation symbol in equation 18 is due to the simplification of the closed-surface integral to the truncated-surface integral caused by a limited receiver aperture. The applied wavefield extrapolation is a model-driven method that means that the Green's functions between all pairs of physical and virtual receivers are calculated based on known baseline models.

Processing sequences

In Figure 2, we schematically illustrate how we conduct the proposed high-frequency localized waveform inversion for time-lapse surveys. We start from the low-frequency baseline full-model FWI aiming at retrieving the long- and medium-wavelength structures (Figure 2a). The inverted models are then interpolated to enable the high-frequency localized FWI. The Green's functions and injection sources (boundary wavefield) are precalculated and stored in preparation for the receiver-side of wavefield extrapolation and source-side injection, respectively, based on the inverted and interpolated baseline models (Figure 2b). In the following section, we explain and verify these processing sequences with various numerical examples.

NUMERICAL EXAMPLES

We first apply the proposed localized waveform inversion scheme to a simple 2D layered-model, then to the more complex 2D Marmousi model, and finally to the 3D SEG-EAGE overthrust model. The 2D layered-model test illustrates the workflow and the capability of the high-frequency localized waveform inversion in retrieving small-scale perturbations. The 2D Marmousi test is to show its strength with more complex velocity models. The 3D test is used to further demonstrate the possibility and efficiency of the high-frequency localized waveform inversion for time-lapse surveys or reservoir monitoring.

A Ricker wavelet is used as the source-time function in the following synthetic tests. All components of the particle velocity wavefield are recorded and inverted. The physical sources and receivers are deployed beneath the upper absorbing boundary without implementing a free-surface boundary condition.

2D layered-model

In the first experiment, we assume that the true baseline model is known (Figure 3a and 3b). The baseline model is uniformly discretized (400 × 200) with a 5 m grid spacing. A Ricker wavelet with a dominant frequency of 20 Hz is used as the source-time function. The time-lapse models shown in Figure 3c and 3d have a thin-layer perturbation ($\Delta V_P = -150$ m/s, $\Delta V_S = -75$ m/s, 10 m thick) inside the injection source boundary (the solid square in Figure 3a and 3b), which is approximately 6% of the average baseline velocity for V_P and V_S. The injection boundary data and the Green's functions between physical and virtual receivers are calculated and stored in advance.

After completing the source-side wavefield injection and receiver-side wavefield extrapolation steps explained in the "Representation

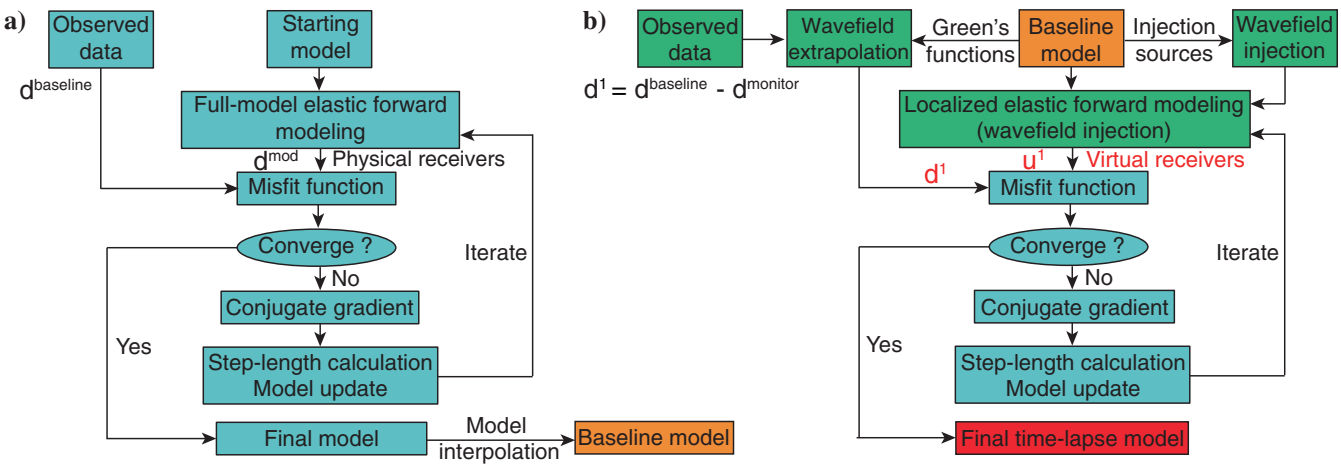


Figure 2. Processing sequences of the proposed high-frequency localized waveform inversion. (a) First, low-frequency full-model elastic waveform inversions to achieve the baseline model. Inverted baseline models are then interpolated to enable the high-frequency localized inversion. (b) Second, the high-frequency localized inversion after wavefield extrapolation and injection based on the interpolated baseline models.

Downloaded from http://pubs.geoscienceworld.org/geophysics/article-pdf/doi/10.1190/geo2020-0286.1/5256644/geo-2020-0286.1.pdf
by CNRS INSU user

theorem for time-lapse wavefield simulation and extrapolation" section, localized waveform inversion can be performed within the target area (the dashed area in Figure 3a and 3b). The inverted V_P and V_S perturbations are shown in Figure 4 after 50 iterations. From the 1D profiles (Figure 4c and 4d), we may notice that the shape of the V_P perturbation is not retrieved as well as that of V_S. This is mainly because the size of the perturbation (10 m) is smaller than the vertical resolution of the P-waves (1/4 wavelength of the P-wave is approximately 30 m at 20 Hz). To better invert a 10 m layer, we may have to further increase the frequency of the forward simulations.

In practice, the true baseline model is never perfectly recovered, especially for short-wavelength structures. Therefore, in the second experiment, we apply the same strategy but starting from a smoothed baseline model (Figure 3e and 3f). The inverted perturbations have the correct shape (Figure 5). However, an apparent vertical shift is observed due to the long- and/or medium-wavelength inaccuracies in the smoothed model (Figure 5c and 5d). This is also why we see the unsymmetrical side lobes in the inverted models.

To improve the baseline model in a long- and medium-wavelength sense (Figure 3e and 3f), we perform a low-frequency (5 Hz central frequency) baseline full-model waveform inversion, which requires a relatively sparse model. Starting from the smoothed baseline layered-model with a sparser grid (100 × 50 with a 20 m grid spacing), we obtain the inverted baseline V_P and V_S models (Figure 6). Due to the sparse grid and the low-frequency content, the sharp boundaries between each layer cannot be fully recovered. But the medium-wavelength structures are more accurate than those in the initial models (the dashed lines in Figure 6c and 6f). To conduct the high-frequency localized waveform inversion for small-scale perturbations, we interpolate the inverted baseline V_P and V_S models to create finer grid (5 m) models. Then, we recalculate and store the injection boundary data and Green's functions for wavefield injection and extrapolation so that we can perform the localized waveform inversion with a 20 Hz central frequency source wavelet. As shown in Figure 7, the vertical shift in Figure 5 is corrected and the thin-layer perturbations are retrieved as well as those found in the first true baseline model experiment.

2D Marmousi model

The layered-model synthetic tests have shown the feasibility and accuracy of the hierarchical waveform inversion method. We further validate the proposed strategy on the more complex Marmousi model. The baseline model is 6 × 1.8 km. The grid spacing is chosen according to the dominant frequency of the source wavelet. For the baseline survey, we aim to retrieve the long- and medium-wavelength structures. Therefore, the grid spacing is set to 30 m, which enables us to perform a relatively low-frequency waveform inversion with a 4 Hz Ricker wavelet as the source. For the subsequent localized waveform inversion, the interpolated model has a 6 m grid spacing and a 25 Hz Ricker wavelet is used as the source-time function. We use 33 shots every 180 m. In total, 171 physical receivers, 12 m in depth, record two components of particle velocity wavefield plus stress wavefield and then are extrapolated to 56 virtual receivers at 980 m in depth. To be more realistic, some small-scale structures are intentionally added into the original true baseline V_P and V_S models (see the black curves in Figure 9c and 9f), so that the low-frequency baseline waveform inversion can retrieve the baseline models to limited accuracy.

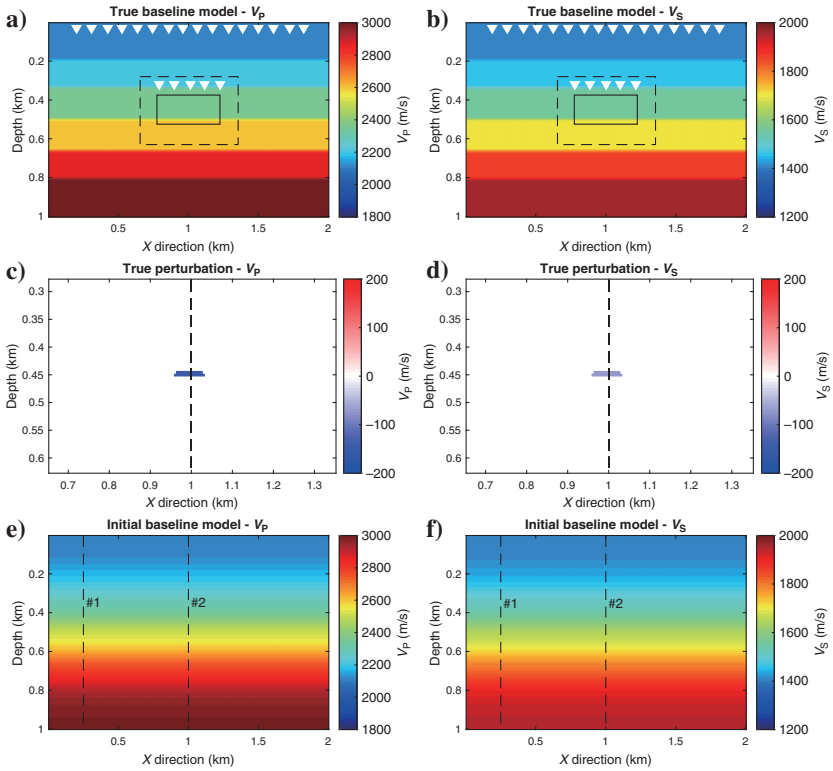


Figure 3. The 2D layered-model tests. True baseline (a) V_P and (b) V_S models. The dashed and solid squares denote the absorbing and injection boundaries for the localized waveform inversion, respectively. The white triangles indicate the depth and aperture of the physical and virtual receivers. True local (c) V_P and (d) V_S perturbations. The initial (e) V_P and (f) V_S models for the baseline waveform inversion.

Downloaded from http://pubs.geoscienceworld.org/geophysics/article-pdf/doi/10.1190/geo2020-0286.1/5256644/geo-2020-0286.1.pdf
by CNRS INSU user

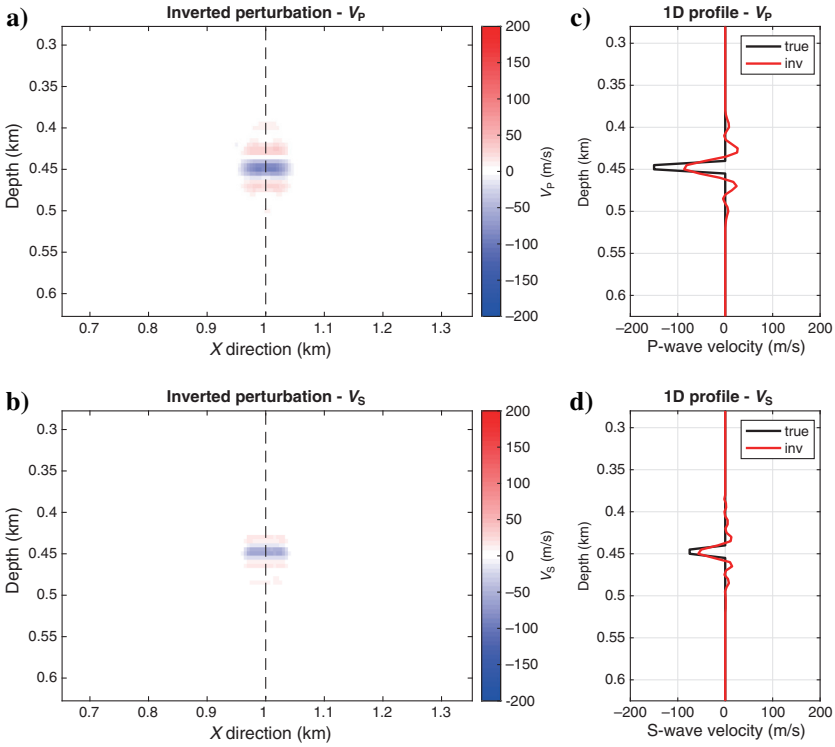


Figure 4. The 2D layered-model localized waveform inversion using the true baseline models. The inverted (a) V_P and (b) V_S perturbations after 50 iterations. (c and d) The 1D profiles of the true and inverted perturbations along the dashed lines in (a and b), respectively.

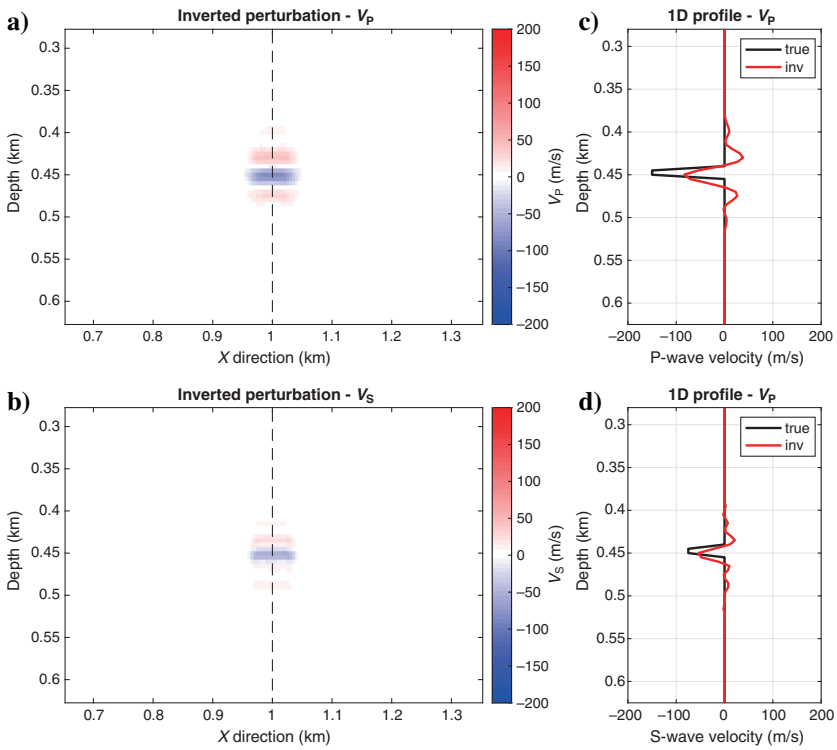


Figure 5. The 2D layered-model localized waveform inversion using the initial smoothed baseline models. (a) Inverted V_P and V_S perturbations after 50 iterations. (c and d) The 1D profiles of the true and inverted perturbations along the dashed lines in (a and b), respectively.

Downloaded from http://pubs.geoscienceworld.org/geophysics/article-pdf/doi/10.1190/geo2020-0286.1/5256644/geo-2020-0286.1.pdf
by CNRS INSU user

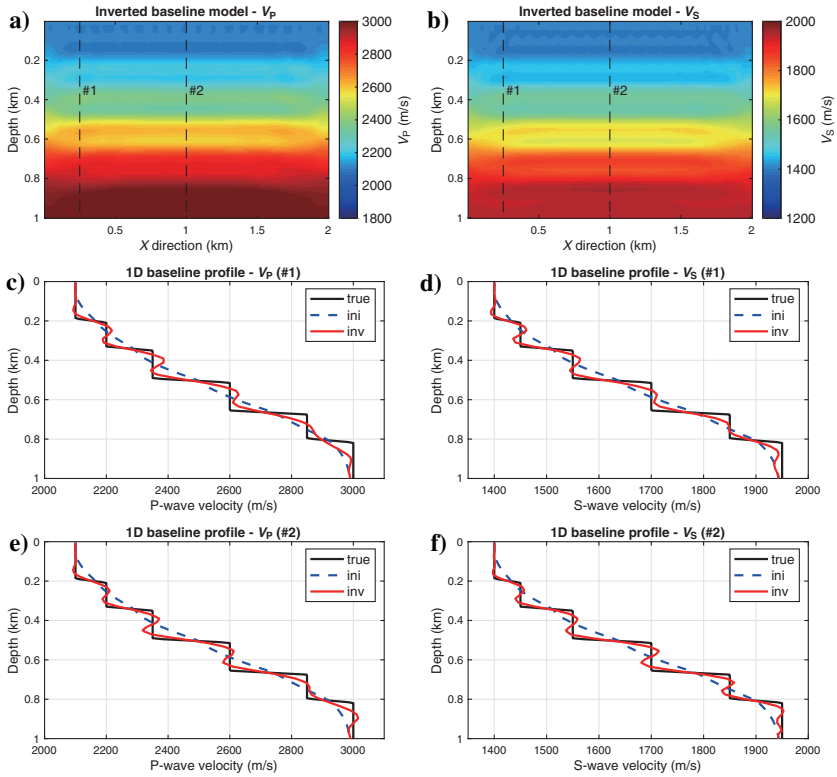


Figure 6. The 2D layered-model baseline waveform inversion. Inverted baseline (a) V_P and (b) V_S models after 50 iterations. The low-frequency baseline waveform inversion is performed on sparse grid models (spatial interval of 20 m) and then the inverted models are interpolated into denser grid models (spatial interval of 5 m) for subsequent high-frequency localized waveform inversion. The 1D profiles of the true, initial, and inverted baseline (c) V_P and (d) V_S models at location #1. The 1D profiles of the true, initial, and inverted baseline (e) V_P and (f) V_S models at location #2.

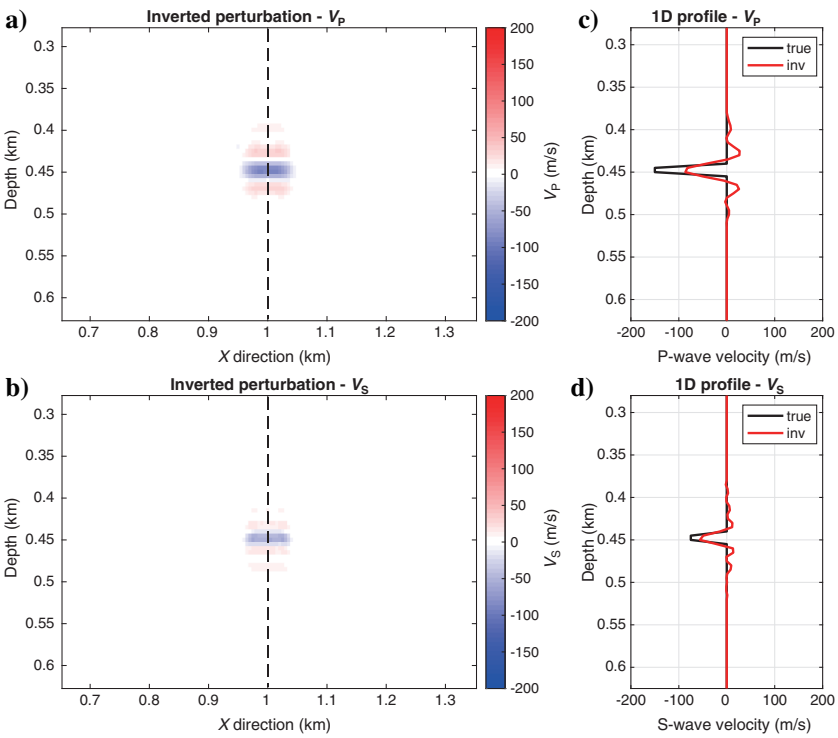


Figure 7. The 2D layered-model localized waveform inversion using inverted baseline models. Inverted (a) V_P and (b) V_S perturbations after 50 iterations. (c and d) The 1D profiles of the true and inverted perturbations along the dashed lines in (a and b), respectively.

Downloaded from http://pubs.geoscienceworld.org/geophysics/article-pdf/doi/10.1190/geo2020-0286.1/5256644/geo-2020-0286.1.pdf
by CNRS INSU user

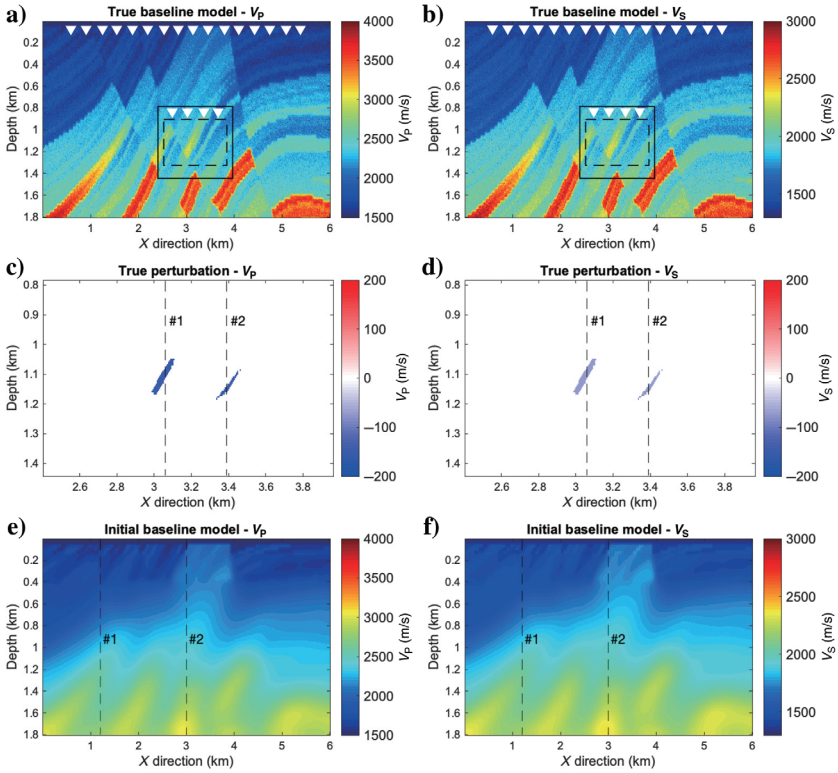


Figure 8. The 2D Marmousi model tests. The true baseline (a) V_P and (b) V_S models. The white triangles indicate the depth and aperture of the physical and virtual receivers. The true local (c) V_P and (d) V_S perturbations. The initial (e) V_P and (f) V_S models for the low-frequency baseline waveform inversion.

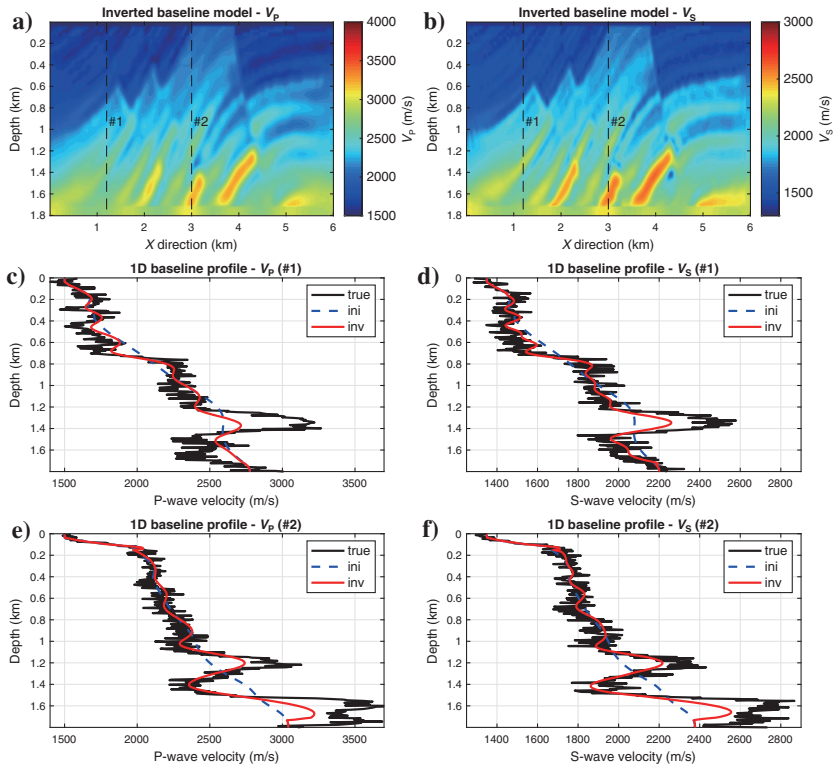


Figure 9. The 2D Marmousi baseline waveform inversion. Inverted baseline (a) V_P and (b) V_S models after 50 iterations. The 1D profile of the inverted Marmousi baseline (c) V_P and (d) V_S models at location #1. The 1D profiles of the true, initial, and inverted Marmousi baseline (e) V_P and (f) V_S models at location #2.

Downloaded from http://pubs.geoscienceworld.org/geophysics/article-pdf/doi/10.1190/geo2020-0286.1/5256644/geo-2020-0286.1.pdf
by CNRS INSU user

The true and initial models for the baseline waveform inversion are shown in Figure 8a, 8b, 8e, and 8f, respectively. Figure 9 displays the inverted baseline models with the corresponding 1D velocity profiles after 50 iterations. As expected, the inverted baseline V_P and V_S models have generally accurate long- and medium-wavelength contents. With the inverted V_P and V_S models from the low-frequency baseline waveform inversion, the subsequent localized waveform inversion is capable of recovering small-scale perturbations as shown in Figure 10.

The data and residuals (the vertical velocity component) from one shot located in the middle of the model are shown in Figure 11. The extrapolated time-lapse data difference, which also represents the initial residuals (Figure 11a), contains some spurious events (see the arrows in Figure 11) caused by the inaccurate Green's functions

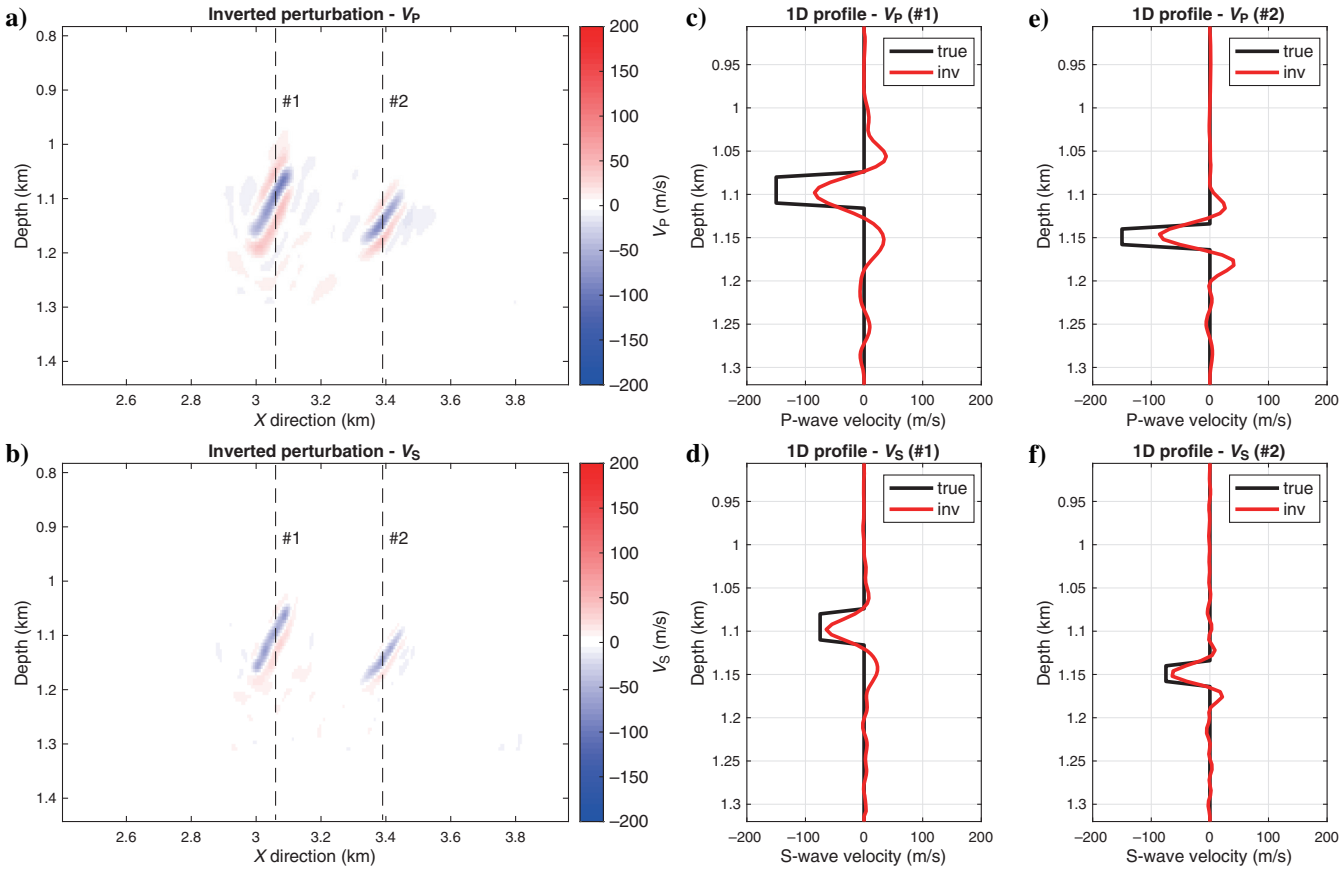
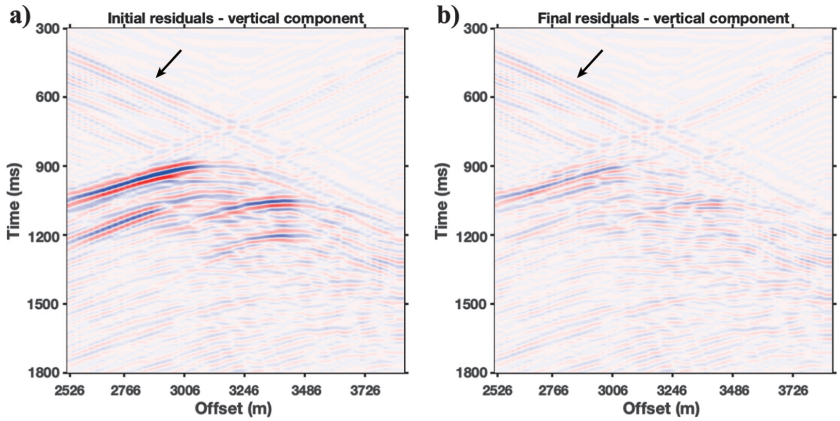


Figure 10. The 2D Marmousi model localized waveform inversion using inverted baseline models. The inverted (a) V_P and (b) V_S perturbations after 50 iterations. (c and e) The 1D profiles of the true and inverted V_P perturbations along the dashed lines 1 and 2 in (a), respectively. (d and f) The 1D profiles of the true and inverted V_S perturbations along the dashed lines 1 and 2 in (b), respectively.`

Figure 11. Initial and final residuals of one selected shot in the 2D Marmousi model localized waveform inversion after 50 iterations. (a) The initial residuals (the extrapolated wavefield) of the vertical velocity component. (b) The final residuals. The arrows point to the spurious events, which are mainly caused by the wavefield extrapolation. Both plots use the same clip value for display.



Downloaded from http://pubs.geoscienceworld.org/geophysics/article-pdf/doi/10.1190/geo2020-0286.1/5256644/geo-2020-0286.1.pdf
by CNRS INSU user

and the truncated integral when applying the correlation-type representation theorem. From the final residuals (Figure 11b), we can see that the residuals related to the true time-lapse changes (hyperbola-shaped events) are mostly reduced whereas the extrapolation errors (earlier events before 900 ms) do not affect the inversion results. This is because the wavefield injection method naturally serves as an anticausal filter, which ensures that nonphysical residuals do not get mapped into the inverted models.

3D SEG-EAGE overthrust model

To verify the possibility and efficiency of our localized waveform inversion to 4D seismic, we apply the same strategy to the 3D SEG-EAGE overthrust model with comparisons to the double-difference full-model waveform inversion method. In particular, we impose a preconditioning to the time-lapse full-model inversion, which only allows the gradient update to happen in the same target area as in the localized inversion. The true, initial, and inverted baseline models ($2 \times 2 \times 2$ km) are shown in Figure 12. In total, 7396 (86×86 in X- and Y-directions) physical receivers are placed at 40 m in depth with regular spacing of 20 m and 961 virtual receivers are placed at 850 m in depth with the same spatial interval. Ricker wavelets with a dominant frequency of 5 and 13 Hz are used as the source term for the full-model baseline and localized waveform inversion, respectively. In total, 16 sources are placed at 20 m in depth with a source interval of 400 m. The selected 2D profiles ($Y = 1$ km) of the true baseline models, true perturbations, and initial baseline models are shown in Figure 13. Figure 14 shows the 2D profiles ($Y = 1$ km) of the inverted 3D baseline models from the low-frequency full-model inversion after 30 iterations and their corresponding 1D velocity profiles.

The selected profiles of the 3D perturbations obtained from the localized inversions using the inverted baseline model are shown in Figure 15a and 15b. The corresponding 1D profiles are shown in Figure 15c and 15d. Comparing the FWI model with a preconditioning (Figure 16), the localized inversion retrieves similar results after the same number of iterations (30) as expected. The data residuals (the horizontal velocity component) of the localized and full-model waveform inversion from one shot ($X = Y = 0.8$ km) are shown in Figures 17 and 18, respectively. The initial residuals of the localized inversion (Figure 17a) are actually the extrapolated time-lapse data differences at the target level and are possibly mixed with extrapolation artifacts, whereas those of the full-model inversion (Figure 18a) are calculated at the surface and consist of the pure target-related time-lapse data differences. Although the same preconditioning on the area of gradient updates is implemented for the full-model and localized inversions, the reduced data set after wavefield extrapolation may additionally affect the step-length calculation and make the convergence rate of the localized inversion slightly faster than that of the full-model inversion.

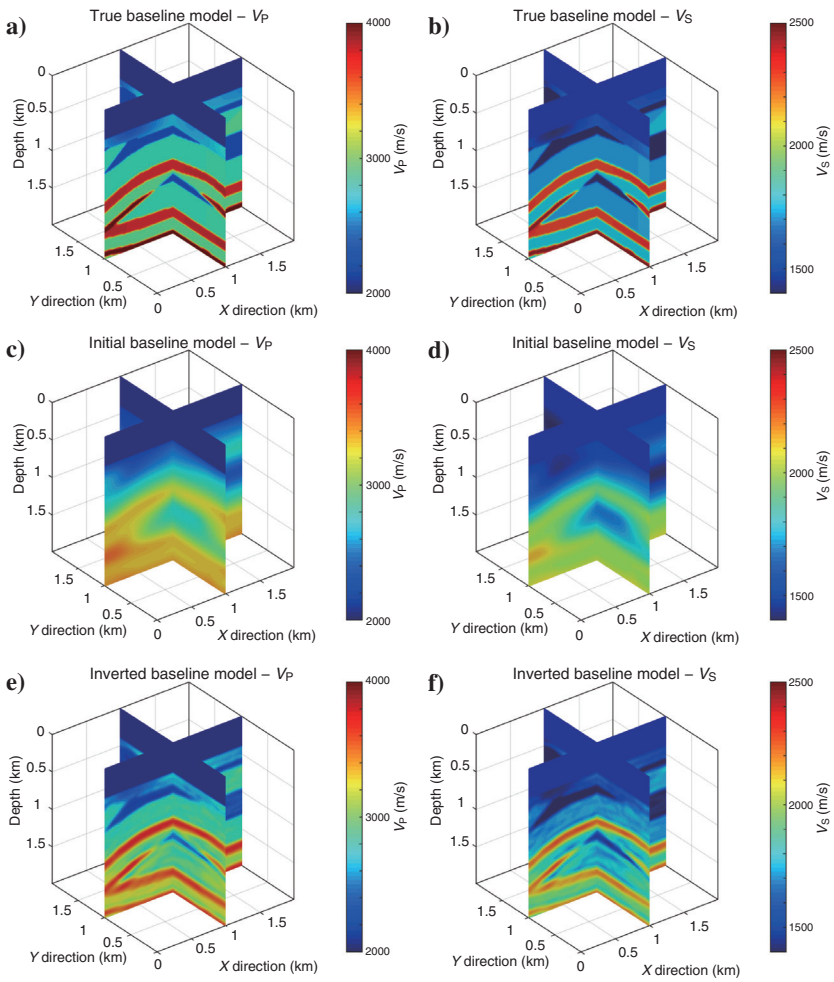


Figure 12. The 3D SEG-EAGE overthrust model tests. The true baseline (a) V_P and (b) V_S models. Initial (c) V_P and (d) V_S models for the baseline waveform inversion. The inverted (e) V_P and (f) V_S baseline models after 30 iterations.

Downloaded from http://pubs.geoscienceworld.org/geophysics/article-pdf/doi/10.1190/geo2020-0286.1/5256644/geo-2020-0286.1.pdf
by CNRS INSU user

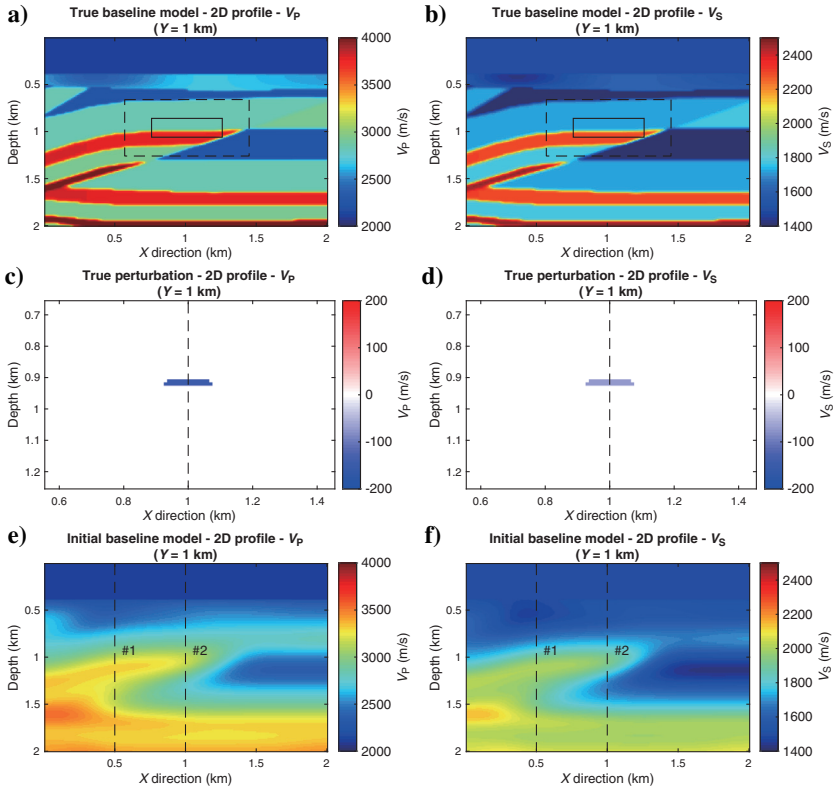


Figure 13. The 2D profiles of 3D SEG-EAGE overthrust models. The 2D profiles of the true baseline (a) V_P and (b) V_S models at 1 km in the Y-direction. The dashed and solid squares denote the absorbing and the injection boundary for localized waveform inversion, respectively. The 2D profiles of the true local (c) V_P and (d) V_S perturbations. The 2D profiles of the initial (e) V_P and (f) V_S models for the baseline waveform inversion.

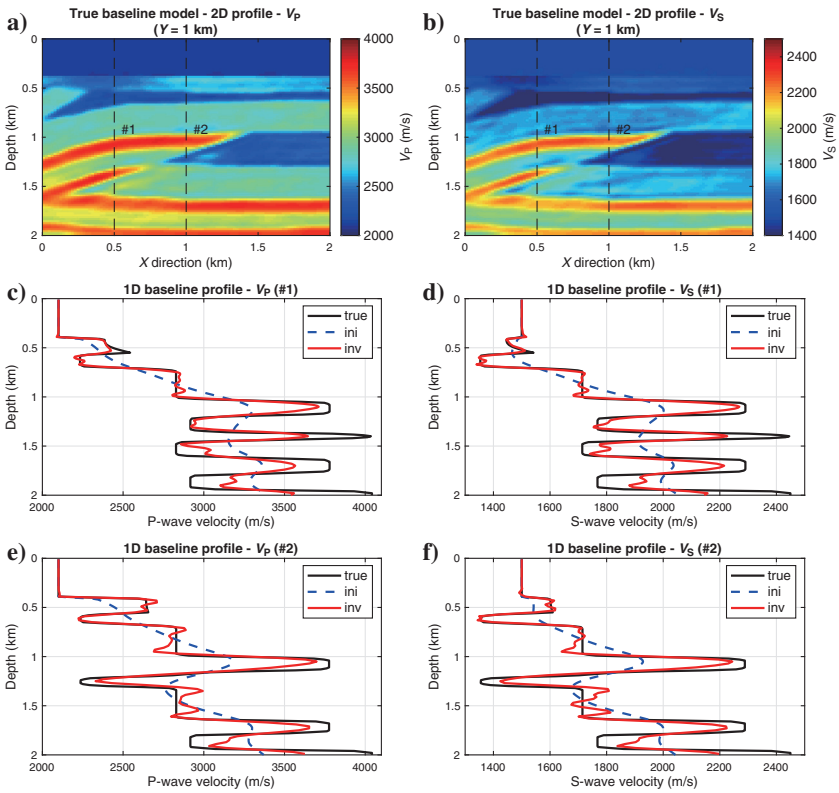


Figure 14. The 2D profiles of the inverted 3D SEG-EAGE overthrust models. The 2D profiles of the inverted baseline (a) V_P and (b) V_S models after 30 iterations. The 1D profiles of the true, initial, and inverted baseline (c) V_P and (d) V_S models at location #1. The 1D profiles of the true, initial, and inverted baseline (e) V_P and (f) V_S models at location #2.

Downloaded from http://pubs.geoscienceworld.org/geophysics/article-pdf/doi/10.1190/geo2020-0286.1/5256644/geo-2020-0286.1.pdf
by CNRS INSU user

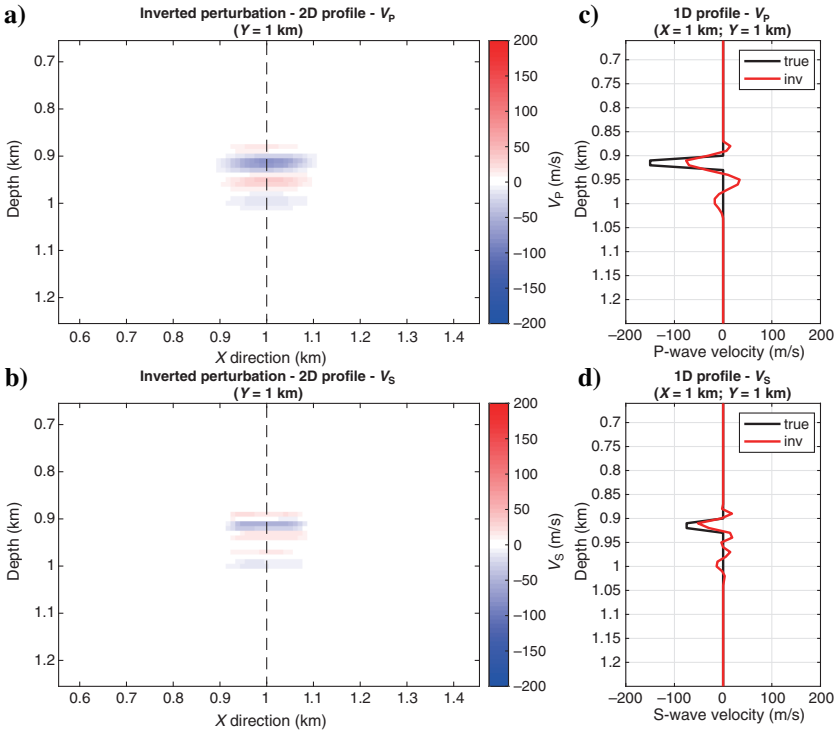


Figure 15. The 3D SEG-EAGE overthrust localized waveform inversion using the inverted baseline models. The 2D profiles of the inverted (a) V_P and (b) V_S perturbations after 30 iterations. (c and d) The 1D profiles of the true and inverted perturbations along the dashed lines in (a and b), respectively.

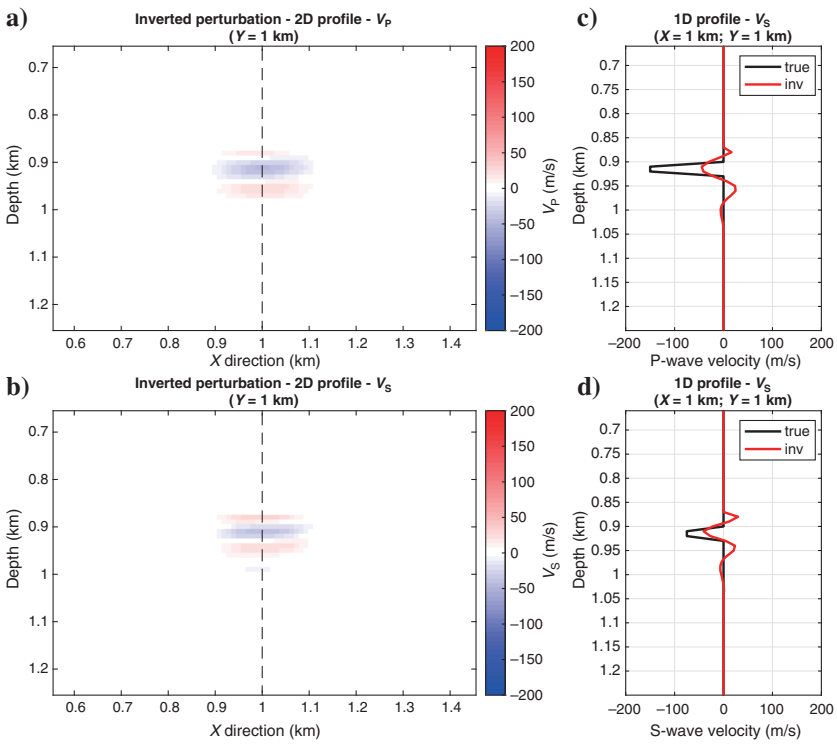


Figure 16. The 3D SEG-EAGE overthrust full-model waveform inversion using the inverted baseline models. The 2D profiles of inverted (a) V_P and (b) V_S perturbations after 30 iterations. (c and d) The 1D profiles of the true and inverted perturbations along the dashed lines in (a and b), respectively.

Downloaded from http://pubs.geoscienceworld.org/geophysics/article-pdf/doi/10.1190/geo2020-0286.1/5256644/geo-2020-0286.1.pdf
by CNRS INSU user

The comparison of computational costs between the full model and the localized waveform inversion for the 3D test is given in Table 1. Compared to the conventional full-model inversion, we need extra calculation and storage of Green's functions and injection sources, where the total number of forward simulations equals the number of virtual receivers multiplied by three (the three components of extrapolated data) plus the number of physical sources. These precalculated Green's functions and injection sources can be reused for multivintages of 4D surveys in ideal cases. The wavefield extrapolation will help focus the inversion on the target level without going back and forth between physical and virtual receivers. As shown in Table 1, we approximately speed up the computation by a factor of 11. Even though we take into account the cost of wavefield injection and extrapolation, which can be roughly ignored in time-lapse seismic surveys with several vintages, a speed-up factor of 4.1 is still attractive. Meanwhile, the memory requirements (RAM) are reduced by a factor of 4.5. The savings in terms of computing time and RAM can be further enhanced with the increasing frequency band and the ratio between the size of the baseline and the localized models. Hard disk storage for the localized inversion is increased by a factor of 2.2 to store the injection sources and Green's functions. However, this is not a critical problem because hard disk space is less expensive and easier to expand than RAM.

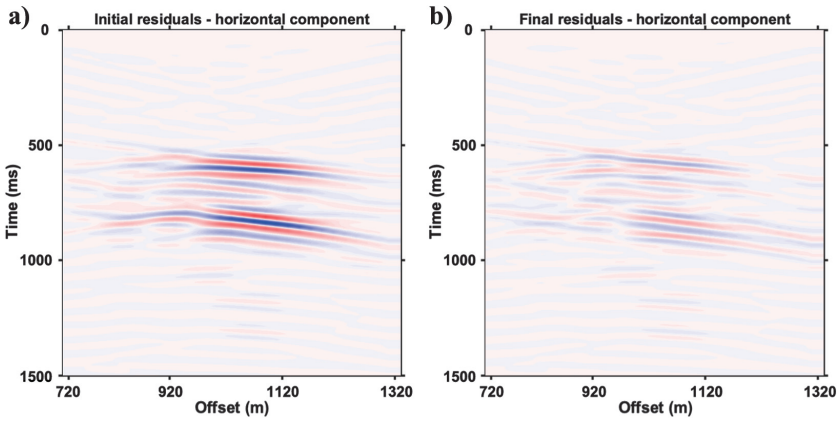


Figure 17. The initial and final residuals of one selected shot in the 3D overthrust localized inversion after 30 iterations. (a) The initial residuals (the extrapolated wavefield) of the horizontal velocity component. (b) The final residuals. Both plots are using the same clip value for display.

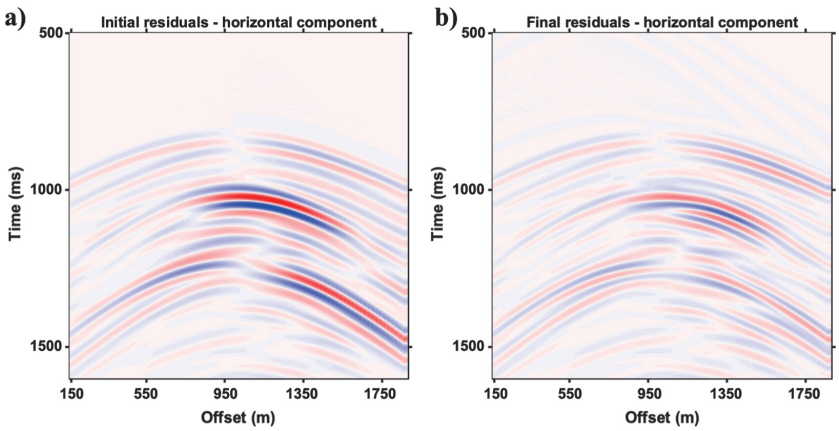


Figure 18. The initial and final residuals of one selected shot in the 3D overthrust double-difference full-model inversion with a gradient preconditioning after 30 iterations. (a) The initial residuals of the horizontal velocity component. (b) The final residuals. Both plots use the same clip value for display.

Table 1. Comparison of computational costs between the full-model and localized waveform inversion in the 3D SEG-EAGE overthrust model for 30 iterations.

	CPU time (hours)	RAM (Gb)	Hard disk (Gb)
Full-model FWI (1)	≈9.70	≈58.0	≈2.20
Injection + extrapolation (2)	≈1.47	—	—
Localized FWI (3)	≈0.88	≈13.0	≈16.0
(1)/(3)	≈11.0	≈4.50	≈0.14
(1)/(2 + 3)	≈4.10	—	—

DISCUSSION

There are several approximations made in the applications of representation theorem to the source-side wavefield injection and the receiver-side extrapolation. For the source-side, we neglect the high-order interactions between the inside scattered wavefields and outside structures (van Manen et al., 2007). For the receiver side, the truncated surface integral will lead to the single-sided illumination problem (Wapenaar et al., 1989; Wapenaar and Fokkema, 2006). More advanced techniques, such as the exact boundary condition for the source side and Marchenko redatuming for the receiver side, are expected to improve the accuracy of localized forward modeling and wavefield extrapolation (van Manen et al., 2007; Broggini et al., 2017; Ravasi, 2017). However, most of them will cause additional cost, which may degrade the efficiency of localized FWI, especially in 3D elastic cases. Therefore, we stick to the conventional wavefield injection method and nonrecursive correlation-based wavefield extrapolation in this study.

Increasing the frequency contents for waveform inversion may pose theoretical and practical challenges. From a theoretical point of view, it may aggravate the nonlinearity and ill-posedness of the inverse problem. From a practical point of view, solving large-scale high-frequency 3D

Downloaded from http://pubs.geoscienceworld.org/geophysics/article-pdf/doi/10.1190/geo2020-0286.1/5256644/geo-2020-0286.1.pdf
by CNRS INSU user

elastic waveform inversion problems is still too expensive considering the current computing facilities. In this study, we primarily focus on practical aspects and try to reduce the computational cost of 4D elastic waveform inversion to a more acceptable level with a local inversion method. We do not address here other common concerns, such as noise effects and crosstalk issues when dealing with FWI. It is not that they are nonexistent in localized inversions, but they are not specifically caused by the localization of FWI. Furthermore, any improvement that aims at alleviating theoretical issues, such as modifying objective functions, optimal parameterization, and multiscale strategy, can be straightforwardly adopted by the proposed localized inversion scheme.

Various scale structural changes may occur during oil/gas production, but normally they are expected to appear at different time scales. Small-scale structural changes that occur in the target area are more promptly introduced by production activities than are large-scale perturbations (e.g., subsidence). In this study, we are trying to show that, with a relatively accurate long- to medium-wavelength baseline model, we can invert for the short-term small-scale changes in the target area efficiently and accurately, despite the outside small-scale unknown perturbations. In cases of large-scale perturbations in the overburden, we have to conduct a classic full-model waveform inversion to correct our knowledge of the long-wavelength structures of the monitor model. If we neglect them, the inverted local perturbations might be inaccurate as shown in the 2D layered-model test.

CONCLUSION

The main objective of the localized high-frequency waveform inversion is to reduce the computational cost so that we can better exploit high-quality broadband seismic records and efficiently estimate the small-scale physical properties of subsurface structures (<10 m). We introduce a hierarchical localized elastic waveform inversion scheme for 3D time-lapse surveys, and we successfully apply it to different synthetic data sets. The first low-frequency full-model inversion to retrieve baseline models requires sparse grids, contributing to the reduction of computational time and the second localized inversion can further mitigate the computational cost. Due to the reduced modeling area, localized inversions can be performed on significantly finer grids, which allows using a broader seismic bandwidth, compared to conventional full-model inversion. The inverted baseline model is sufficiently accurate for the high-frequency localized waveform inversion, although it is only long- and medium-wavelength equivalent to the true model. The significantly reduced cost in terms of memory and computing time in 3D localized FWI shows its potential in the application to time-lapse seismic and high-resolution reservoir monitoring.

ACKNOWLEDGMENTS

The research described in this paper was carried out as a part of the Paris Exploration Geophysics Group project funded by the French National Research Agency, CGG, TOTAL, and Schlumberger. A significant part of the calculations in this work was performed on S-CAPAD at the Institut de physique du globe de Paris. We thank B. Willemsen, A. Guitton, A. Baumstein, J. Shragge, and two anonymous reviewers for their constructive and valuable comments, which greatly improved our manuscript. This is Institut de physique du globe de Paris contribution 4198.

DATA AND MATERIALS AVAILABILITY

Data associated with this research are available and can be obtained by contacting the corresponding author.

REFERENCES

Asnaashari, A., R. Brossier, S. Garambois, F. Audebert, P. Thore, and J. Virieux, 2015, Time-lapse seismic imaging using regularized full-waveform inversion with a prior model: Which strategy? Geophysical Prospecting, **63**, 78–98, doi: 10.1111/1365-2478.12176.

Bojarski, N. N., 1983, Generalized reaction principles and reciprocity theorems for the wave equations, and the relationship between the time-advanced and time-retarded fields: The Journal of the Acoustical Society of America, **74**, 281–285, doi: 10.1121/1.389721.

Borisov, D., and S. C. Singh, 2015, Three-dimensional elastic full waveform inversion in a marine environment using multicomponent ocean-bottom cables: A synthetic study: Geophysical Journal International, **201**, 1215–1234, doi: 10.1093/gji/ggv048.

Borisov, D., S. C. Singh, and N. Fuji, 2015, An efficient method of 3-D elastic full waveform inversion using a finite-difference injection method for time-lapse imaging: Geophysical Journal International, **202**, 1908–1922, doi: 10.1093/gji/ggv268.

Broggini, F., M. Vasmel, J. O. Robertsson, and D.-J. van Manen, 2017, Immersive boundary conditions: Theory, implementation, and examples: Geophysics, **82**, no. 3, T97–T110, doi: 10.1190/geo2016-0458.1.

Capdeville, Y., E. Chaljub, and J. P. Montagner, 2003, Coupling the spectral element method with a modal solution for elastic wave propagation in global earth models: Geophysical Journal International, **152**, 34–67, doi: 10.1046/j.1365-246X.2003.01808.x.

Claerbout, J. F., 1985, Imaging the earth's interior: Blackwell Scientific Publications.

Eriksrud, M., 2014, Seabed permanent reservoir monitoring (PRM) — A valid 4D seismic technology for fields in the North Sea: First Break, **32**, 67–73.

Fink, M., D. Cassereau, A. Derode, C. Prada, P. Roux, M. Tanter, J.-L. Thomas, and F. Wu, 2000, Time-reversed acoustics: Reports on Progress in Physics, **63**, 1933–1995, doi: 10.1088/0034-4885/63/12/202.

Gardner, G., L. Gardner, and A. Gregory, 1974, Formation velocity and density — The diagnostic basics for stratigraphic traps: Geophysics, **39**, 770–780, doi: 10.1190/1.1440465.

Geller, R. J., and T. Hara, 1993, Two efficient algorithms for iterative linearized inversion of seismic waveform data: Geophysical Journal International, **115**, 699–710, doi: 10.1111/j.1365-246X.1993.tb01488.x.

Graves, R. W., 1996, Simulating seismic wave propagation in 3D elastic media using staggered-grid finite differences: Bulletin of the Seismological Society of America, **86**, 1091–1106.

Haffinger, P., A. Gisolf, and P. V. D. Berg, 2013, Towards high resolution quantitative subsurface models by full waveform inversion: Geophysical Journal International, **193**, 788–797, doi: 10.1093/gji/ggt021.

Hicks, E., H. Hoeber, M. Houbiers, S. P. Lescoffit, A. Ratcliffe, and V. Vinje, 2016, Time-lapse full-waveform inversion as a reservoir-monitoring tool — A North Sea case study: The Leading Edge, **35**, 850–858, doi: 10.1190/tle35100850.1.

Hoeber, H., E. Hicks, M. Houbiers, S. Pannetier-Lescoffit, A. Ratcliffe, and V. Vinje, 2017, 4D full waveform inversion — A North Sea case study: First Workshop on Practical Reservoir Monitoring, EAGE, Extended Abstracts, cp–505, doi: 10.3997/2214-4609.201700026.

Jack, I., 2017, 4D seismic — Past, present, and future: The Leading Edge, **36**, 386–392, doi: 10.1190/tle36050386.1.

Jannane, M., W. Beydoun, E. Crase, D. Cao, Z. Koren, E. Landa, M. Mendes, A. Pica, M. Noble, G. Roeth, and S. Singh, 1989, Wavelengths of earth structures that can be resolved from seismic reflection data: Geophysics, **54**, 906–910, doi: 10.1190/1.1442719.

Knopoff, L., and A. F. Gangi, 1959, Seismic reciprocity: Geophysics, **24**, 681–691, doi: 10.1190/1.1438647.

Komatitsch, D., and R. Martin, 2007, An unsplit convolutional perfectly matched layer improved at grazing incidence for the seismic wave equation: Geophysics, **72**, no. 5, SM155–SM167, doi: 10.1190/1.2757586.

Lailly, P., 1983, The seismic inverse problem as a sequence of before stack migrations: Conference on inverse scattering — Theory and application: SIAM, **11**, 206.

Landrø, M., 2006, Future challenges and unexplored methods for 4D seismic analysis: CSEG Recorder, **31**, 128–135.

Landrø, M., and J. Stammeijer, 2004, Quantitative estimation of compaction and velocity changes using 4D impedance and traveltime changes: Geophysics, **69**, 949–957, doi: 10.1190/1.1778238.

Levander, A. R., 1988, Fourth-order finite-difference P-SV seismograms: Geophysics, **53**, 1425–1436, doi: 10.1190/1.1442422.

Downloaded from http://pubs.geoscienceworld.org/geophysics/article-pdf/doi/10.1190/geo2020-0286.1/5256644/geo-2020-0286.1.pdf
by CNRS INSU user

Liu, Q., and J. Tromp, 2006, Finite-frequency kernels based on adjoint methods: Bulletin of the Seismological Society of America, **96**, 2383–2397, doi: 10.1785/0120060041.
Lumley, D. E., 2004, Business and technology challenges for 4D seismic reservoir monitoring: The Leading Edge, **23**, 1166–1168, doi: 10.1190/1.1825942.
Malcolm, A., and B. Willemsen, 2016, Rapid 4D FWI using a local wave solver: The Leading Edge, **35**, 1053–1059, doi: 10.1190/tle35121053.1.
Marjanović, M., R.-É. Plessix, A. Stopin, and S. C. Singh, 2018, Elastic versus acoustic 3-D full waveform inversion at the East Pacific Rise 9° 50' N: Geophysical Journal International, **216**, 1497–1506, doi: 10.1093/gji/ggy503.
Masson, Y., P. Cupillard, Y. Capdeville, and B. Romanowicz, 2013, On the numerical implementation of time-reversal mirrors for tomographic imaging: Geophysical Journal International, **196**, 1580–1599, doi: 10.1093/gji/ggt459.
Masson, Y., and B. Romanowicz, 2017, Box tomography: Localized imaging of remote targets buried in an unknown medium, a step forward for understanding key structures in the deep earth: Geophysical Journal International, **211**, 141–163, doi: 10.1093/gji/ggx141.
Monteiller, V., S. Chevrot, D. Komatitsch, and N. Fuji, 2012, A hybrid method to compute short-period synthetic seismograms of teleseismic body waves in a 3-D regional model: Geophysical Journal International, **192**, 230–247, doi: 10.1093/gji/ggs006.
Monteiller, V., S. Chevrot, D. Komatitsch, and Y. Wang, 2015, Three-dimensional full waveform inversion of short-period teleseismic wavefields based upon the SEM–DSM hybrid method: Geophysical Journal International, **202**, 811–827, doi: 10.1093/gji/ggv189.
Mora, P., 1987, Nonlinear two-dimensional elastic inversion of multioffset seismic data: Geophysics, **52**, 1211–1228, doi: 10.1190/1.1442384.
Opršal, I., C. Matyska, and K. Irikura, 2009, The source-box wave propagation hybrid methods: General formulation and implementation: Geophysical Journal International, **176**, 555–564, doi: 10.1111/j.1365-246X.2008.03986.x.
Pica, A., J. Diet, and A. Tarantola, 1990, Nonlinear inversion of seismic reflection data in a laterally invariant medium: Geophysics, **55**, 284–292, doi: 10.1190/1.1442836.
Plessix, R.-E., 2006, A review of the adjoint-state method for computing the gradient of a functional with geophysical applications: Geophysical Journal International, **167**, 495–503, doi: 10.1111/j.1365-246X.2006.02978.x.
Polak, E., 1971, Computational methods in optimization: A unified approach. Academic Press.
Pratt, R. G., 1999, Seismic waveform inversion in the frequency domain — Part 1: Theory and verification in a physical scale model: Geophysics, **64**, 888–901, doi: 10.1190/1.1444597.
Queißer, M., and S. C. Singh, 2013, Full waveform inversion in the time lapse mode applied to CO_2 storage at Sleipner: Geophysical Prospecting, **61**, 537–555, doi: 10.1111/j.1365-2478.2012.01072.x.
Raknes, E. B., and B. Arntsen, 2015, A numerical study of 3D elastic time-lapse full-waveform inversion using multicomponent seismic data: Geophysics, **80**, no. 6, R303–R315, doi: 10.1190/geo2014-0472.1.
Ravasi, M., 2017, Rayleigh-Marchenko redatuming for target-oriented, true-amplitude imaging: Geophysics, **82**, no. 6, S439–S452, doi: 10.1190/geo2017-0262.1.
Robertsson, J. O., and C. H. Chapman, 2000, An efficient method for calculating finite-difference seismograms after model alterations: Geophysics, **65**, 907–918, doi: 10.1190/1.1444787.
Shipp, R. M., and S. C. Singh, 2002, Two-dimensional full wavefield inversion of wide-aperture marine seismic streamer data: Geophysical Journal International, **151**, 325–344, doi: 10.1046/j.1365-246X.2002.01645.x.
Snieder, R., S. Hubbard, M. Haney, G. Bawden, P. Hatchell, A. Revil, and D. G. M. W. Group, 2007, Advanced noninvasive geophysical monitoring techniques: Annual Review of Earth and Planetary Sciences, **35**, 653–683, doi: 10.1146/annurev.earth.35.092006.145050.
Tarantola, A., 1984, Inversion of seismic reflection data in the acoustic approximation: Geophysics, **49**, 1259–1266, doi: 10.1190/1.1441754.
Tarantola, A., 1986, A strategy for nonlinear elastic inversion of seismic reflection data: Geophysics, **51**, 1893–1903, doi: 10.1190/1.1442046.
van Manen, D.-J., J. O. Robertsson, and A. Curtis, 2007, Exact wave field simulation for finite-volume scattering problems: The Journal of the Acoustical Society of America, **122**, EL115–EL121, doi: 10.1121/1.2771371.
Virieux, J., 1986, P-SV wave propagation in heterogeneous media: Velocity-stress finite-difference method: Geophysics, **51**, 889–901, doi: 10.1190/1.1442147.
Virieux, J., and S. Operto, 2009, An overview of full-waveform inversion in exploration geophysics: Geophysics, **74**, no. 6, WCC1–WCC26, doi: 10.1190/1.3238367.
Waldhauser, F., and W. L. Ellsworth, 2000, A double-difference earthquake location algorithm: Method and application to the northern Hayward fault, California: Bulletin of the Seismological Society of America, **90**, 1353–1368, doi: 10.1785/0120000006.
Wapenaar, C., G. Peels, V. Budejicky, and A. Berkhout, 1989, Inverse extrapolation of primary seismic waves: Geophysics, **54**, 853–863, doi: 10.1190/1.1442714.
Wapenaar, K., and J. Fokkema, 2006, Green's function representations for seismic interferometry: Geophysics, **71**, no. 4, SI33–SI46, doi: 10.1190/1.2213955.
Willemsen, B., and A. Malcolm, 2017, An efficient coupled acoustic-elastic local solver applied to phase inversion: Geophysics, **82**, no. 4, R219–R234, doi: 10.1190/geo2016-0572.1.
Yang, D., F. Liu, S. Morton, A. Malcolm, and M. Fehler, 2016, Time-lapse full-waveform inversion with ocean-bottom-cable data: Application on Valhall field: Geophysics, **81**, no. 4, R225–R235, doi: 10.1190/geo2015-0345.1.
Yang, D., M. Meadows, P. Inderwiesen, J. Landa, A. Malcolm, and M. Fehler, 2015, Double-difference waveform inversion: Feasibility and robustness study with pressure data: Geophysics, **80**, no. 6, M129–M141, doi: 10.1190/geo2014-0489.1.
Yao, Z., and G. F. Margrave, 2000, Elastic wavefield modelling in 3D by fourth-order staggered-grid finite difference technique: CREWES Research Report, 12, 1–10.
Yuan, S., N. Fuji, S. Singh, and D. Borisov, 2017a, Localized time-lapse elastic waveform inversion using wavefield injection and extrapolation: 2-D parametric studies: Geophysical Journal International, **209**, 1699–1717, doi: 10.1093/gji/ggx118.
Yuan, S., N. Fuji, S. Singh, and D. Borisov, 2017b, Towards high resolution localised elastic full waveform inversion: 79th Annual International Conference and Exhibition, EAGE, Extended Abstracts, 1–5, doi: 10.3997/2214-4609.201700509.
Zheng, Y., P. Barton, and S. Singh, 2011, Strategies for elastic full waveform inversion of time-lapse ocean bottom cable (OBC) seismic data: 81st Annual International Meeting, SEG, Expanded Abstracts, 4195–4200, doi: 10.1190/1.3628083.

Biographies and photographs of the authors are not available.

Downloaded from http://pubs.geoscienceworld.org/geophysics/article-pdf/doi/10.1190/geo2020-0286.1/5256644/geo-2020-0286.1.pdf
by CNRS INSU user